



KELT-11 b: Abundances of Water and Constraints on Carbon-bearing Molecules from the Hubble Transmission Spectrum

Q. Changeat¹ , B. Edwards¹ , A. F. Al-Refaie , M. Morvan , A. Tsiaras , I. P. Waldmann , and G. Tinetti 

Department of Physics and Astronomy, University College London, Gower Street, WC1E 6BT London, UK; quentin.changeat.18@ucl.ac.uk

Received 2020 June 25; revised 2020 September 8; accepted 2020 October 2; published 2020 November 13

Abstract

In the past decade, the analysis of exoplanet atmospheric spectra has revealed the presence of water vapor in almost all the planets observed, with the exception of a fraction of overcast planets. Indeed, water vapor presents a large absorption signature in the wavelength coverage of the Hubble Space Telescope's (HST) Wide Field Camera 3 (WFC3), which is the main space-based observatory for atmospheric studies of exoplanets, making its detection very robust. However, while carbon-bearing species such as methane, carbon monoxide, and carbon dioxide are also predicted from current chemical models, their direct detection and abundance characterization has remained a challenge. Here we analyze the transmission spectrum of the puffy, clear hot-Jupiter KELT-11 b from the HST WFC3 camera. We find that the spectrum is consistent with the presence of water vapor and an additional absorption at longer wavelengths than $1.5 \mu\text{m}$, which could well be explained by a mix of carbon bearing molecules. CO_2 , when included is systematically detected. One of the main difficulties to constrain the abundance of those molecules is their weak signatures across the HST WFC3 wavelength coverage, particularly when compared to those of water. Through a comprehensive retrieval analysis, we attempt to explain the main degeneracies present in this data set and explore some of the recurrent challenges that are occurring in retrieval studies (e.g., the impact of model selection, the use of free versus self-consistent chemistry, and the combination of instrument observations). Our results make this planet an exceptional example of a chemical laboratory to test current physical and chemical models of the atmospheres of hot Jupiters.

Unified Astronomy Thesaurus concepts: [Exoplanet atmospheres \(487\)](#); [Extrasolar gas giants \(509\)](#); [Bayesian statistics \(1900\)](#); [Exoplanet atmospheric composition \(2021\)](#)

1. Introduction

Transmission and emission spectroscopy have formed the cornerstone of exoplanet atmospheric characterization, enabling the discovery of water in many planets (Tinetti et al. 2007; Crouzet et al. 2014; Tsiaras et al. 2018). While the detection of water is now routine for the hot-Jupiter class of planets, other molecules such as the carbon species remains challenging with current space instrumentation. With a few exceptions (Swain et al. 2008, 2009), most claims for the carbon species from space have been based on additional absorption in the infrared Spitzer photometric bands (Madhusudhan et al. 2010; Line et al. 2016; Stevenson et al. 2017; Gandhi et al. 2019) or from ground-based observations using either direct imaging (Macintosh et al. 2015; Barman et al. 2015; Lacour et al. 2019) or high-dispersion techniques (Snellen et al. 2010; de Kok et al. 2013; Konopacky et al. 2013; Brogi et al. 2017). While very valuable, these detections often lack a reference baseline or require the combination of multiple instruments, each with different systematics, which may limit the determination of absolute abundances or may lower the detection significance (Brogi & Line 2019; Yip et al. 2020).

To analyze those exoplanet spectra, inverse retrieval techniques are often used (Rodgers 2000; Irwin et al. 2008; Madhusudhan & Seager 2009; Line et al. 2013; Waldmann et al. 2015b, 2015a; Al-Refaie et al. 2019; Gandhi et al. 2019; Mollière et al. 2019; Zhang et al. 2019; Min et al. 2020). These techniques explore the information content in an exoplanet spectrum and map the parameter space of possible solutions. In the last few years, it has become a standard practice to perform

atmospheric retrievals using self-consistent chemical models as opposed to free chemical models. In free retrievals, the chemical composition of the atmosphere is retrieved using parametric profiles, which are not assuming prior knowledge. For example profiles can be assumed constant with altitude or use more complex parametric descriptions when required (Parmentier et al. 2018; Changeat et al. 2019). Self-consistent models rely on simplifying assumptions (atmosphere in thermochemical equilibrium) to reduce the number of free parameters in the model and provide a more complex chemical structure (variation of chemistry with altitude). For exoplanets, it remains a strong assumption of the physical and chemical state of the atmosphere that can lead to strong biases (Venot et al. 2015; Changeat et al. 2019, 2020; Anisman et al. 2020).

The planet KELT-11 b was discovered in 2016 orbiting a bright G star ($K_{\text{mag}} = 6.122$), with an orbital period of 4.736 days (Pepper et al. 2017). Due to its very low density (0.093 g cm^{-3}), it was immediately associated with a very large scale height and was predicted to become one of the benchmark planets for atmospheric characterization. Further observations from the ground and the Spitzer Space Telescope refined the orbital and star parameters (Beatty et al. 2017). A recent paper (Zák et al. 2019) analyzed the high-resolution data from the High Accuracy Radial Velocity Planet Searcher (HARPS) in the search for sodium, hydrogen, and lithium. They saw no evidence for these species, and they attributed the nondetection to the possible presence of high-altitude clouds. They also reported a low stellar activity of the host star, a result obtained by monitoring the Ca I and Mg I lines.

Here we present the analysis of a single transit of KELT-11 b from the Hubble Space Telescope (HST). We first describe the

¹ These authors contributed equally to this work.

way our analysis was carried using the public pipeline Iraclis and the public retrieval code TauREx3. Then we show the results from our free exploration of the atmospheric properties, showing that multiple solutions can reflect the information content in this spectrum. We then discuss the use of self-consistent chemical models in atmospheric retrievals and the combination of observations using the complementary TESS data. Our results are also compared with a recent independent analysis of the same data set from Colón et al. (2020).

2. Methodology

2.1. Extraction of Planetary Spectrum

A single transit of KELT-11 b was taken with the G141 grism (1.088–1.68 μm) of the Wide Field Camera 3 (WFC3) in 2018 April (PN: 15225, PI: Knicole Colon). We obtained the publicly available data from the HST Mikulski Archive for Space Telescopes (MAST) archive² We used our publicly available tools to perform the end-to-end analysis from the raw data to the atmospheric parameters. The HST data was reduced, and the light curves fitted, using the Iraclis software (Tsiaras et al. 2016b). We then used our Bayesian retrieval code TauREx3 (Al-Refaie et al. 2019) to extract and analyze the molecular content of this atmosphere.

The visit consisted of nine HST orbits with the G141 infrared grism of the WFC3 camera (1.088–1.68 μm), in the spatial scanning mode. During an exposure using the spatial scanning mode the instrument slews along the cross-dispersion direction, allowing for longer exposure times and increased signal-to-noise ratio without the risk of saturation (Deming et al. 2013). Both forward (increasing row number) and reverse (decreasing row number) scanning were used for these observations to increase the duty cycle.

The detector settings were SUBTYPE = SQ512SUB, SAMP_{SEQ} = SPARS25, NSAMP = 4, and APERTURE = GRISM512, and the scanning speed was 0''96s⁻¹. The final images had a total exposure time of 46.695518 s, a maximum signal level of 36,000 electrons per pixel and a total scanning length of 51''312. For calibration purposes, a 2.559081 s nondispersed (direct) image of the target was taken at the beginning of each orbit, using the F130N filter and the following settings: SUBTYPE = SQ512SUB, SAMP_{SEQ} = RAPID, NSAMP = 4, and APERTURE = GRISM512.

We carried out the analysis of the transit using Iraclis, our highly specialized software for processing WFC3 spatially scanned spectroscopic images (Tsiaras et al. 2016b, 2016a, 2018, 2019). The reduction process included the following steps: zero-read subtraction, reference-pixel correction, non-linearity correction, dark current subtraction, gain conversion, sky background subtraction, calibration, flat-field correction, and bad-pixel/cosmic-ray correction. Then we extracted the white (1.088–1.68 μm) and spectral light curves from the reduced images, taking into account the geometric distortions caused by the tilted detector of the WFC3 infrared channel.

We fitted the light curves using our transit model package PyLightcurve, with the transit parameters from Beatty et al. (2017) and limb-darkening coefficients calculated based on the PHOENIX (Allard et al. 2012) model (see tables in Appendix A), the nonlinear formula, and the stellar parameters, also from Beatty et al. (2017). These were computed using

ExoTETHyS (Morello et al. 2020). During our fitting of the white light curve, the planet-to-star radius ratio and the mid-transit time were the only free parameters, along with a model for the systematics (Kreidberg et al. 2014; Tsiaras et al. 2016b).

It is common for WFC3 exoplanet observations to be affected by two kinds of time-dependent systematics: the long-term and short-term ramps (e.g., Kreidberg et al. 2015; Evans et al. 2016; Line et al. 2016). The first affects each HST visit and usually has a linear behavior, while the second affects each HST orbit and is modeled as having an exponential behavior. The formula we used for the white light curve systematics (R_w) was

$$R_w(t) = n_w^{\text{scan}}(1 - r_a(t - T_0))(1 - r_{b1}e^{-r_{b2}(t-t_o)}), \quad (1)$$

where t is time, n_w^{scan} is a normalization factor, T_0 is the mid-transit time, t_o is the time when each HST orbit starts, r_a is the slope of a linear systematic trend along each HST visit, and (r_{b1} , r_{b2}) are the coefficients of an exponential systematic trend along each HST orbit. The normalization factor we used (n_w^{scan}) was changed to n_w^{for} for upward scanning directions (forward scanning) and to n_w^{rev} for downward scanning directions (reverse scanning). The reason for using different normalization factors is the slightly different effective exposure time due to the known upstream/downstream effect (McCullough & MacKenty 2012).

We fitted the white light curves using the formulae above and the uncertainties per pixel, as propagated through the data reduction process. However, it is common in HST/WFC3 data to have additional scatter that cannot be explained by the ramp model. For this reason, we scaled up the uncertainties in the individual data points, for their median to match the standard deviation of the residuals, and repeated the fitting (Tsiaras et al. 2018). We found orbital parameters from the literature (Beatty et al. 2017) to provide an excellent fit to the data and thus the only free parameters in our white fitting, other than the HST systematics, were the mid-transit time and the planet-to-star radius ratio. We show the white light curve fitting resulting from our spectrum extraction step in Figure 1.

In our analysis, we found that the measured mid-transit time had drifted from the expected ephemeris. We therefore used this observation, along with data from the Transiting Exoplanet Satellite (TESS; Ricker et al. 2014), to refine the ephemeris of KELT-11 b.

Next, we fitted the spectral light curves (see Figure 2) with a transit model (with the planet-to-star radius ratio being the only free parameter) along with a model for the systematics (R_λ) that included the white light curve (divide-white method; Kreidberg et al. 2014) and a wavelength-dependent, visit-long slope (Tsiaras et al. 2016b),

$$R_\lambda(t) = n_\lambda^{\text{scan}}(1 - \chi_\lambda(t - T_0))\frac{LC_w}{M_w}, \quad (2)$$

where χ_λ is the slope of a wavelength-dependent linear systematic trend along each HST visit, LC_w is the white light curve, and M_w is the best-fit model for the white light curve. Again, the normalization factor we used (n_λ^{scan}) was changed to (n_λ^{for}) for upward scanning directions (forward scanning) and to (n_λ^{rev}) for downward scanning directions (reverse scanning). Also, in the same way as for the white light curves, we performed an initial fit using the pipeline uncertainties and then

² <https://archive.stsci.edu/hst/search.php>

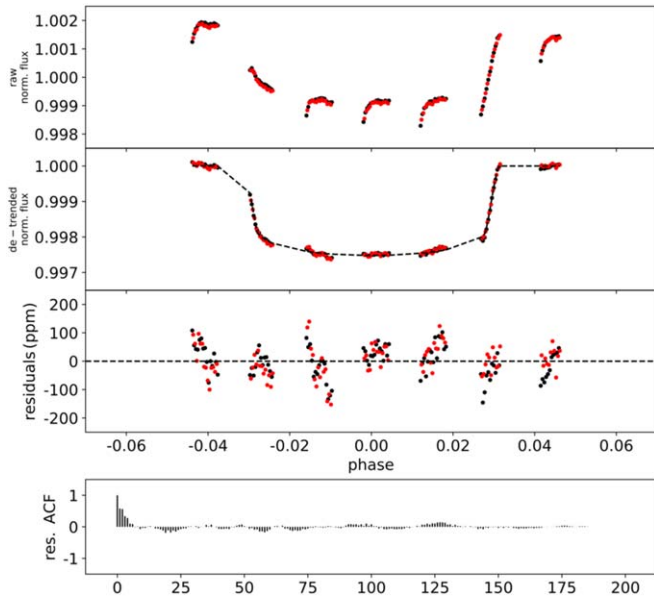


Figure 1. White light curve fit for the transit of KELT-11 b. First panel: raw light curve, after normalization. Second panel: light curve, divided by the best-fit model for the systematics. Third panel: residuals for best-fit model. Fourth panel: autocorrelation function of the residuals. Black data points are for forward scans while data from the reverse scans are indicated in red.

refitted while scaling these uncertainties up, for their median to match the standard deviation of the residuals. The final extracted spectrum is given in Appendix B.

2.2. Spitzer Transit Observation

A transit observation was taken with Spitzer’s Infrared Camera Array (IRAC) at $3.6\ \mu\text{m}$ (PID: 12096, PI: T. Beatty). We decided not to include it in this present analysis because, as stated in Beatty et al. (2017), the transit occurred earlier than expected, meaning the pre-ingress part of the light curve is missing. As the ramp effect is especially pronounced during the settling of IRAC observations (see, e.g., Agol et al. 2010), the preprocessing of this light curve by any of the standard detrending techniques (e.g., Morvan et al. 2020) would likely lead to larger uncertainties in the retrieved transit depth.³ This would in turn reduce the chances of a robust combination between observations from the different instruments (Bruno et al. 2020; Yip et al. 2020).

2.3. TESS Data Reduction and Ephemeris Refinement

Accurate knowledge of exoplanet transit times is crucial for atmospheric studies. To ensure that KELT-11 b can be observed in the future, we used the HST white light curve mid-time, along with data from TESS, to update the ephemeris of the planet. TESS data is publicly available through the MAST archive and we use the pipeline from Edwards et al. (2020b) to download, clean, and fit the 2 minute cadence pre-search data conditioning (PDC) light curves (Smith et al. 2012; Stumpe et al. 2012, 2014). KELT-11 b was studied in Sector 9 and, after excluding bad data, we recovered five transits. These were fitted individually with the planet-to-star radius ratio R_p/R_s , reduced semimajor axis (a/R_s), inclination (i), and transit mid-time (T_0) as free parameters. The observed minus calculated (O–C) residuals are shown in Figure 3 along with the

³ In fact, the initial exposures of exoplanet light curves with Spitzer, where the telescope is settling, are often discarded on account of the steepest ramps on these portions.



Figure 2. Spectral light curves fitted with Iraclis for the transmission spectra where, for clarity, an offset has been applied. Left: the detrended spectral light curves with best-fit model plotted. Right: residuals from the fitting with values for the Chi-squared (χ^2), the standard deviation of the residuals with respect to the photon noise ($\bar{\sigma}$), and the autocorrelation (AC).

detrended data, the best-fit model, and the residuals for each transit. We calculated the ephemeris to be $P = 4.73620495 \pm 0.00000086$ days and $T_0 = 2458260.168608 \pm 0.000030$ BJD_{TDB} where P is the period, T_0 is the mid-time of the transit, and BJD_{TDB} is the barycentric Julian date in the barycentric dynamical time standard. The mid-times used and the updated parameters are given in Table 1.

2.4. Retrieval Setup

The observed spectrum (Appendix B) was analyzed using our Bayesian retrieval framework TauREx 3 (Waldmann et al. 2015b, 2015a; Al-Refaie et al. 2019; A. F. Al-Refaie et al. 2020, in preparation), which was recently benchmarked (Barstow et al. 2020) against the other retrieval codes NEMESIS (Irwin et al. 2008) and CHIMERA (Line et al. 2013). We utilized the absorption cross-sections from the ExoMol database (Tennyson & Yurchenko 2012; Tennyson et al. 2016, 2020; Chubb et al. 2020) and explored the parameter space with the algorithm

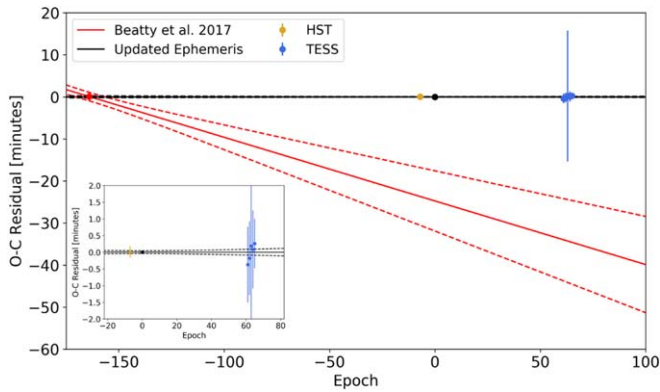


Figure 3. O–C residuals for KELT-11 b. The ephemeris of the literature (Beatty et al. 2017) are shown in red, the HST transit in gold, and the TESS data in blue. The black line denotes the new ephemeris of this work with the dashed lines showing the associated 1σ uncertainties. The inset shows a zoomed plot to highlight the accuracy of the transit times measured here. We note that the third TESS light curve had a high uncertainty on the transit mid-time due to an interruption in the observation which caused egress to be missed.

Table 1

Transit Mid-times Used to Refine the Ephemeris of KELT-11 b in This Work

Epoch	Transit Mid-time (BJD _{TDB})	Reference
–164	2457483.431 ± 0.0007	Beatty et al. (2017)
–7	2458227.015148 ± 0.000111	This Work
61	2458549.077357 ± 0.000524	This Work
62	2458553.813428 ± 0.000616	This Work
63	2458558.54938 ± 0.006887	This Work
64	2458563.285654 ± 0.000481	This Work
65	2458568.021737 ± 0.000486	This Work
Derived Values		
Period (P)	4.73620495 ± 0.00000086	days
Transit mid-time (T_0)	2458260.168608 ± 0.000030	BJD _{TDB}

MultiNest (Feroz et al. 2009) with 750 live points and an evidence tolerance of 0.5. We adopted uniform priors for all the free parameters.

Our atmosphere is a one-dimensional model consisting of 100 layers, covering the pressures from 10 bar to 10^{-9} bar, equally spaced in log-scale. For the trace gases we considered the molecules H_2O (Barton et al. 2017; Polyansky et al. 2018), CH_4 (Hill et al. 2013; Yurchenko & Tennyson 2014), CO (Li et al. 2015), CO_2 (Rothman et al. 2010), C_2H_2 (Wilzewski et al. 2016), C_2H_4 (Mant et al. 2018), HCN (Barber et al. 2013; Harris et al. 2006), TiO (McKemmish et al. 2019), VO (McKemmish et al. 2016), and FeH (Bernath 2020).

In order to avoid biases from chemical assumptions, we considered free chemistry for the main result section. For completeness and due to the particularly high signal-to-noise ratio of the KELT-11 b spectrum, we still discuss the case of equilibrium chemistry in the discussion section. In free chemistry, we fit each of the molecule abundances in volume mixing ratios with log-prior bounds from -12 to -1 . The rest of the atmosphere is composed of H_2 and He for which the ratio is fixed to solar values. On top of the molecular absorption, we include opacity from Rayleigh scattering (Cox 2015) and collision-induced absorption (CIA) processes from H_2 – H_2 (Abel et al. 2011) and H_2 – He (Abel et al. 2012) pairs. The planetary mass was fixed to

the literature values in all the performed retrievals, since it is poorly constrained by HST observations (Changeat et al. 2020).

In order to model clouds we included a Grey opacity—a fully opaque atmosphere above a given pressure—and attempted to recover the top pressure of this cloud deck P_c . Finally, we fit for the planet radius R_p at 10 bar with bounds $0.9 R_J - 1.6 R_J$ and an isothermal temperature profile T with bounds 500 K–2500 K. In transit, the temperature affects mostly the atmospheric scale height and the narrow wavelength range of HST does not allow the recovery of the thermal structure precisely (Rocchetto et al. 2016; Changeat et al. 2019).

In the results section, we investigate the information that can be extracted from this spectrum by running several free retrieval models:

1. A base retrieval composed of water and the main carbon based molecules (CH_4 , CO , and CO_2). It is a conservative model as the considered molecules are expected to be present in the atmosphere of KELT-11 b (Section 3.1).

2. An extended retrieval model. Since the observed spectrum contains additional absorption in the longer wavelengths, we investigate a larger range of carbon compounds. HCN , C_2H_2 , and C_2H_4 are added to the base setup (Section 3.2).

3. A water-only retrieval, which only contains absorption from water vapor (Section 3.3). This allows us to statistically assess the relevance of the carbon bearing specie detections in the base and extended models.

4. A full retrieval scenario, which also includes the near-optical absorbers TiO , VO , and FeH . This addition was motivated from studying the combined TESS and HST spectrum (Section 3.4).

For model comparison, we provide the relative global log evidence ($\log E$) of each solution in Table 2. These are relative to a standard flat line model ($\log E_{\text{flat}} = 146.6$) built by removing all wavelength-dependent absorption and fitting only the radius, temperature, and clouds (Tsiasar et al. 2018). In the discussion section, we provide complementary retrievals with the aim to use KELT-11 b as an example to illustrate particular aspects of retrieval study:

1. The atmospheric chemical equilibrium (ACE) retrieval uses an equilibrium chemistry scheme from Agúndez et al. (2014). For this run, the only two chemical free parameters are the metallicity ($\log M$) and the C/O ratio (Section 4.1).

2. A combined retrieval is also performed. This uses the full setup on a spectrum combining the HST spectrum with the TESS photometric point (Section 4.2).

3. Results

From our retrieval exploration, we find that the free models provide a reasonable fit to the observed spectrum. Figure 4 compares the best-fit spectra for all the considered retrievals. Similarly, Table 2 provides a summary of the retrieved parameters for each model as well as the global log evidence relative to the flat line model. This indicator describes the significance to which an atmospheric signal is detected and allows us to compare the tested models (Kass & Raftery 1995; Tsiasar et al. 2018).

The selection of the best model, among the ones tested, is difficult since their respective $\log E$ lie within the same range (variations of less than three). The full model provides the best statistical fit but is only marginally better than the other solutions. In all the tested scenarios, the temperature seems

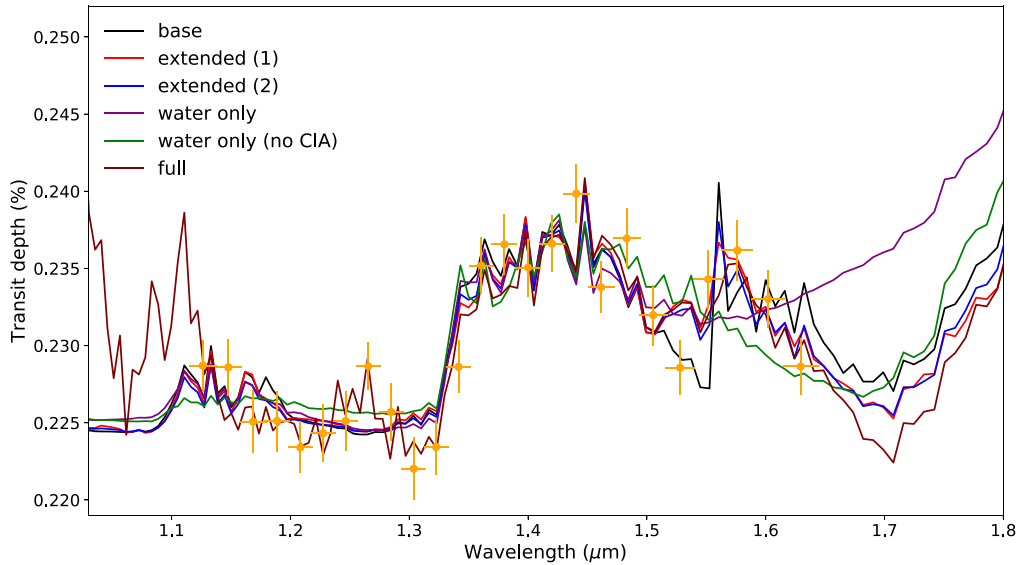


Figure 4. Comparison of the best-fit spectra from the different retrievals on the KELT-11 b reduced HST data (orange). The feature seen after $1.5 \mu\text{m}$ is better reproduced by models including carbon species but all the models provide a decent fit to this spectrum.

Table 2
Summary of Our Different Retrieval Scenarios

Parameter	Base	Extended (1)	Extended (2)	Water-only	Full	ACE
Rp	$1.19^{+0.01}_{-0.03}$ [1.18]	$1.13^{+0.03}_{-0.04}$ [1.13]	$1.18^{+0.01}_{-0.03}$ [1.14]	$1.18^{+0.01}_{-0.01}$ [1.18]	$1.10^{+0.03}_{-0.05}$ [1.09]	$0.94^{+0.03}_{-0.03}$ [1.01]
T	1334^{+206}_{-167} [1216]	1194^{+188}_{-155} [1169]	1273^{+196}_{-150} [1349]	1423^{+120}_{-83} [1504]	1307^{+172}_{-141} [1347]	2462^{+76}_{-125} [2398]
Pc	$5.0^{+0.7}_{-0.8}$ [4.2]	$2.7^{+0.6}_{-0.6}$ [2.7]	$4.4^{+1.0}_{-0.6}$ [3.6]	$5.2^{+0.5}_{-0.5}$ [4.7]	$2.5^{+0.6}_{-0.9}$ [2.3]	$1.8^{+0.4}_{-0.4}$ [2.9]
log H ₂ O	$-5.9^{+0.4}_{-0.2}$ [-5.3]	$-4.0^{+0.7}_{-0.7}$ [-3.9]	$-5.7^{+0.5}_{-0.3}$ [-5.1]	$-6.2^{+0.1}_{-0.1}$ [-6.2]	$-3.6^{+0.6}_{-0.7}$ [-3.3]	...
log CO	$-3.8^{+1.2}_{-4.3}$ [-2.0]	$-6.9^{+3.4}_{-3.3}$ [-2.3]	$-4.5^{+1.6}_{-4.7}$ [-2.9]	...	$-7.3^{+3.2}_{-2.9}$ [-11.6]	...
log CH ₄	$-9.7^{+1.7}_{-1.6}$ [-7.9]	$-8.4^{+2.2}_{-2.3}$ [-6.4]	$-9.5^{+1.7}_{-1.6}$ [-11.4]	...	$-8.1^{+2.4}_{-2.4}$ [-10.1]	...
log CO ₂	$-6.5^{+1.8}_{-3.7}$ [-4.4]	$-3.0^{+0.7}_{-0.9}$ [-2.7]	$-4.9^{+0.8}_{-4.0}$ [-4.0]	...	$-3.0^{+0.6}_{-2.7}$ [-2.1]	...
log HCN	...	$-4.1^{+0.7}_{-0.7}$ [-4.1]	$-6.5^{+1.1}_{-3.4}$ [-5.4]	...	$-3.7^{+0.7}_{-0.8}$ [-3.5]	...
log C ₂ H ₂	...	$-9.2^{+1.9}_{-1.8}$ [-8.6]	$-9.6^{+1.5}_{-1.5}$ [-10.4]	...	$-8.8^{+2.1}_{-2.0}$ [-8.7]	...
log C ₂ H ₄	...	$-8.6^{+2.2}_{-2.1}$ [-9.5]	$-9.5^{+1.6}_{-1.6}$ [-11.8]	...	$-8.4^{+2.6}_{-2.3}$ [-9.5]	...
log TiO	$-5.1^{+0.6}_{-0.8}$ [-4.9]	...
log VO	$-10.0^{+1.3}_{-1.2}$ [-9.6]	...
log FeH	$-8.8^{+1.7}_{-2.0}$ [-6.6]	...
log M	-0.7 [1.1]	0.4 [1.0]	-1.2 [0.2]	-3.3 [-3.3]	0.4 [1.29]	$0.3^{+0.5}_{-0.7}$ [0.3]
C/O	0.99 [1.00]	0.51 [0.78]	0.76 [0.93]	...	0.53 [0.50]	$0.77^{+0.1}_{-0.3}$ [0.88]
$\Delta \log E$	65.4	66.5	64.9	64.5	66.9	59.3

Note. For each parameter we provide the median and 1σ retrieved parameters as well as the value from the maximum a posteriori (MAP) in bracket. A large difference between the median and the MAP highlights a parameter that did not converge or a non-Gaussian behavior. We also derive the metallicity (log M) and carbon to oxygen ratio (C/O) following MacDonald & Madhusudhan (2019). The last line provides the global log evidence of each retrieval relative to a flat line model. This is built using $\Delta \log E = \log E - \log E_{\text{flat}}$.

consistent (except in the ACE retrieval) around 1300 K. We note that all those solutions agree on the presence of water vapor in the atmosphere of KELT-11 b and that some combination of additional species is necessary to fully explain the peculiar absorption after $1.5 \mu\text{m}$. The recovered abundance of water in our models is subsolar, as also suggested by a recent independent study from Colón et al. (2020). When included in the retrieval, CO₂ is systematically recovered, despite abundances that vary depending on the model considered. For the other species (CO and HCN), their detection depends on the model considered (see the next sections for the details). Here, we detail the four types of retrievals we attempted for this planet.

3.1. Base Retrieval Results

Our first analysis of KELT-11 b uncovers the presence of large molecular signatures in the atmosphere, as seen in the spectral modulations in Figure 5.

More precisely, our base setup detected the presence of water, carbon monoxide, and carbon dioxide. The particularly high signal-to-noise ratio in this data set allows for the extraction of precise constraints on the abundances of these molecules. Our Bayesian analysis (see black posterior distribution in Figure 6) found the abundance of water to be $\log(\text{H}_2\text{O}) = -5.95^{+0.36}_{-0.22}$, the abundance of carbon monoxide to be $\log(\text{CO}) = -3.83^{+1.21}_{-4.34}$, and the abundance of carbon

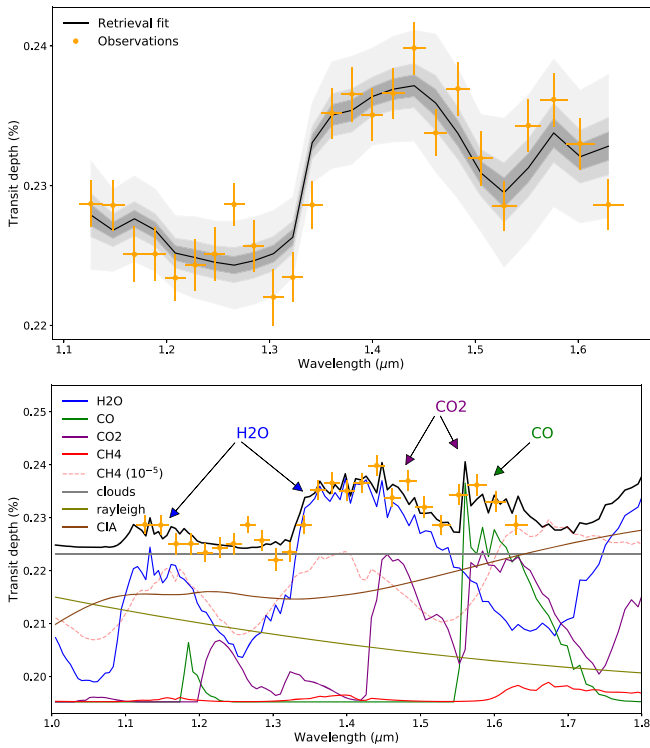


Figure 5. Extracted spectrum of KELT-11 b observed by HST with 1σ error bars (yellow) and fitting results from our base retrieval analysis. Top: best-fit spectrum from our retrieval analysis (black) with the 1σ , 2σ , and 5σ regions (shaded dark). Bottom: best-fit contributions from the different absorbing species. Since CH_4 does not contribute in the best-fit model, we show the contribution it would have for an abundance of 10^{-5} with the dashed red line.

dioxide to be $\log(\text{CO}_2) = -6.53^{+1.78}_{-3.72}$. We note that the recovered water abundance is low, which does not match the expected predictions from theoretical models and other derived abundances from similar planets (Sing et al. 2016; Tsiaras et al. 2018; Pinhas et al. 2019).

From the breakdown of the contributions (bottom part of Figure 5), we deduce that KELT-11 b presents a strong water signature, well defined by the $1.4 \mu\text{m}$ feature, which leads to a very accurate estimation of its abundance. With respect to CO_2 and CO , the signal of these molecules is weaker in the HST wavelength range and possess some similarities. This degeneracy leads to a larger margin of error for the two molecules. However, the additional absorption from $1.4 \mu\text{m}$ to $1.6 \mu\text{m}$ clearly indicates that this model requires a combination of these two molecules. In addition to these three molecules, we also constrain the abundance of methane to be lower than $\log(\text{CH}_4) \lesssim -8$ to 1σ . The updated list of parameters for the atmosphere and the orbit of KELT-11 b is summarized in Table 2.

The recovered temperature is about 1300 K, which is expected since the observations are probing the terminator region, which is naturally colder than the dayside of the planet, better represented by the equilibrium temperature of about 1700 K. Many studies pointed out that these observed differences between equilibrium and terminator temperatures, which are observed for almost all planets (Tsiaras et al. 2018; Skaf et al. 2020), could be caused by three-dimensional biases not accounted for in one-dimensional models (Feng et al. 2016; Caldas et al. 2019; Irwin et al. 2020; Changeat et al. 2020; Changeat & Al-Refaie 2020; Feng et al. 2020; MacDonald et al. 2020; Pluriel et al. 2020).

Contrary to suggestions by Žák et al. (2019), the retrieval presented here indicates a relatively clear atmosphere and does not recover evidence of high-altitude clouds. We constrain the top pressure for the clouds to be $P_c \gtrsim 0.1$ bar. These results could indicate that the atmosphere of KELT-11 b is depleted in sodium and lithium. Other possibilities include a hazy atmosphere, with more opaque absorption at lower wavelengths.

Since methane shares similar features to H_2O , we investigate whether the $1.4 \mu\text{m}$ signal could be from this molecule. Forcing methane to an abundance higher than 10^{-7} highlighted that the stronger absorption shape of methane in the lower ($1.2 \mu\text{m}$) wavelengths (compared to the main $1.4 \mu\text{m}$ feature), as well as the tighter absorption at $1.4 \mu\text{m}$, do not match the spectrum. To explore the significance of this model, we ran several other scenarios that are presented in the next sections.

3.2. Extended Model Results

In the extended model, we add HCN , C_2H_2 , and C_2H_4 , which allows us to explore a wider range of carbon bearing species. As seen in the previous section, the shape of the spectrum at $1.5 \mu\text{m}$ is well fit with CO and CO_2 . However, HCN also shows strong features at $1.5 \mu\text{m}$, which could help the retrieval to fit the observed additional absorption at these wavelengths.

The extended retrieval unveiled two solutions that are highlighted respectively in red and blue in Figure 4 for the spectra and Figure 6 for the posterior distributions.

As opposed to the base solution, Solution 1 does not contain a high abundance of CO but presents better constrained posteriors for CO_2 and HCN , with respective abundances of $-3.1^{+0.7}_{-0.9}$ and $-4.1^{+0.7}_{-0.7}$. The atmosphere is also consistent with the presence of opaque clouds and the recovered water abundance is higher than in the previous run: $-4.0^{+0.7}_{-0.7}$. The breakdown of the contribution from the different molecules for this run can be found in Appendix C. It shows where the additional HCN opacity contributes and illustrates the degeneracies between CO , CO_2 , and HCN . Solution 2 is similar to what was found in the previous section with the base model, when it comes to H_2O , CO , and CO_2 . The atmosphere is consistent with the absorption of H_2O and a mix of carbon bearing species without clouds. There are strong degeneracies between CO , CO_2 , and HCN , where combinations of the three molecules can lead to statistically equally valid solutions. In the posterior distribution of those three molecules, the tails toward the lowest abundances are strong, meaning that their individual detection cannot be fully confirmed. In all runs, the C_2H_2 and C_2H_4 do not contribute to the fit and a upper limit of about 10^{-6} is inferred. The recovered temperature is well constrained and remains similar, in both base and extended solutions, at around 1300 K.

3.3. Water-only Retrieval Results

In order to test the need for CO , CO_2 , and HCN , we perform a complementary retrieval without those molecules (water-only model). The best-fit spectrum is compared with the other runs in Figure 4 (purple), while the posterior distribution is presented in Figure 7.

Results from this run are particularly interesting as they highlight the fact that the water-only model is also a good fit of the observed spectrum. We note that the water-only model only provides a good fit when CIA is included (when CIA is not

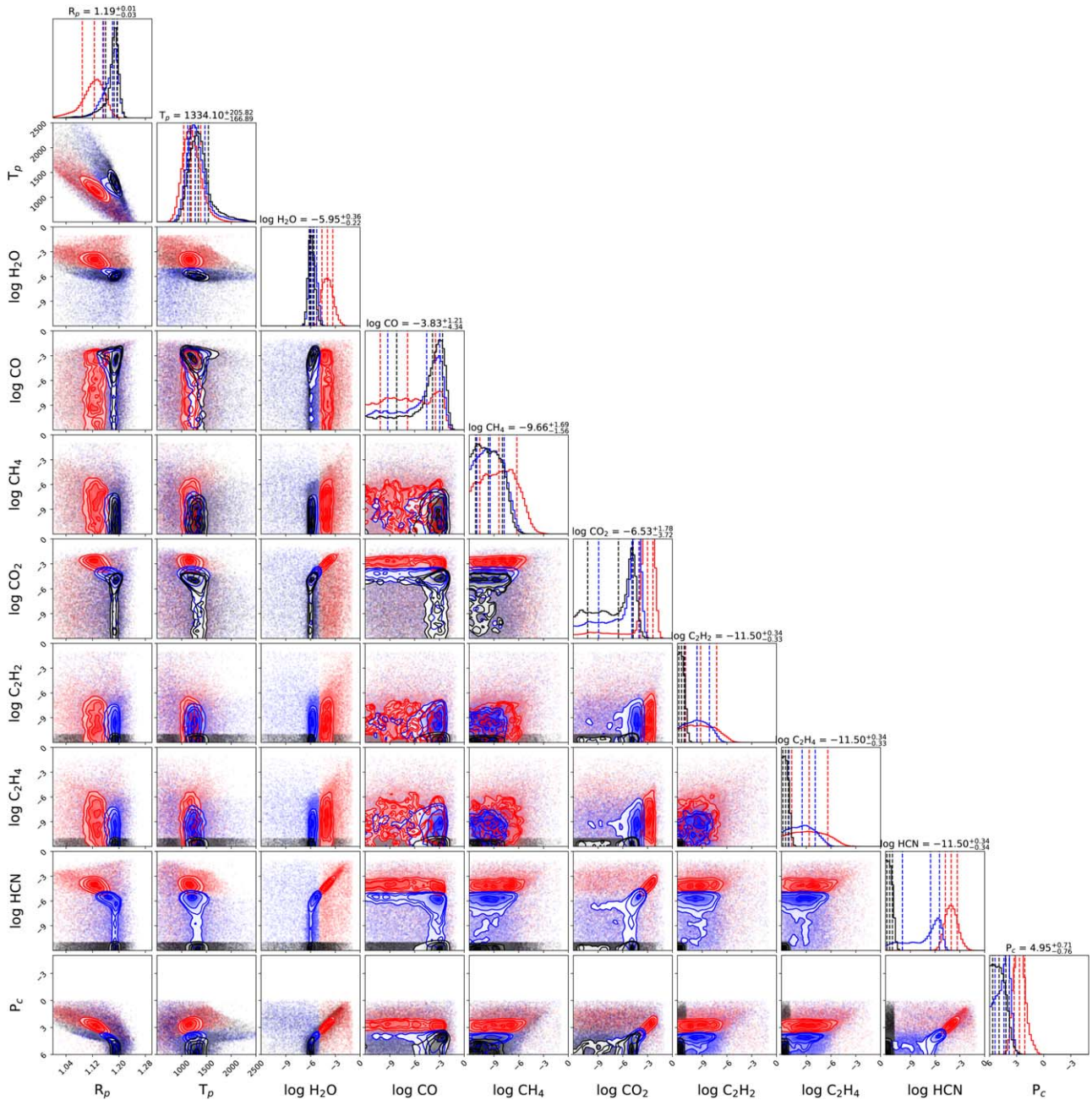


Figure 6. Posterior distributions from our different free retrieval scenarios. Black: base retrieval; red: extended retrieval, solution 1; blue: extended retrieval, solution 2.

included we get $\Delta \log E = 58.7$). The water-only model (no CIA) is shown in green in Figures 4 and 7. In the water-only run, the water abundance drops to $\log(\text{H}_2\text{O}) = -6.2^{+0.1}_{-0.1}$, which is much lower than solar abundances and might be non-physical. The low abundance of water allow CIA to become dominant at longer wavelengths and provide a good fit to the observed signal after $1.5 \mu\text{m}$. The breakdown of the contribution from the different species for the water-only run is presented in Appendix C.

3.4. Full Retrieval

In our full retrieval we also consider the absorption from the optical absorbers: TiO, VO, and FeH. Evidence for these has been presented in a number of previous HST G141

transmission studies (e.g., Edwards et al. 2020a; Skaf et al. 2020). The obtained $\log E$ is higher than with previous models, however it still remains in the same range of evidence: the difference with the water-only model is only 2.4. The spectrum is highlighted in maroon in Figure 4, while the full posterior distribution for this model can be found in Appendix D. As shown in the posterior distribution, the additional flexibility provided by the optical absorbers leads to a different solution. Here, it shows that the HST spectrum can be fit with a much higher abundance of water ($\log \text{H}_2\text{O} = 3.6^{+0.6}_{-0.7}$) associated with $\log \text{TiO} = -5.1^{+0.6}_{-0.8}$. This water mixing ratio is consistent with previously observed abundances for this type of planets (Tsiaras et al. 2018) but the presence of TiO in this atmosphere would be surprising given the recovered temperature of about 1300 K. Additionally, this solution requires a high abundance

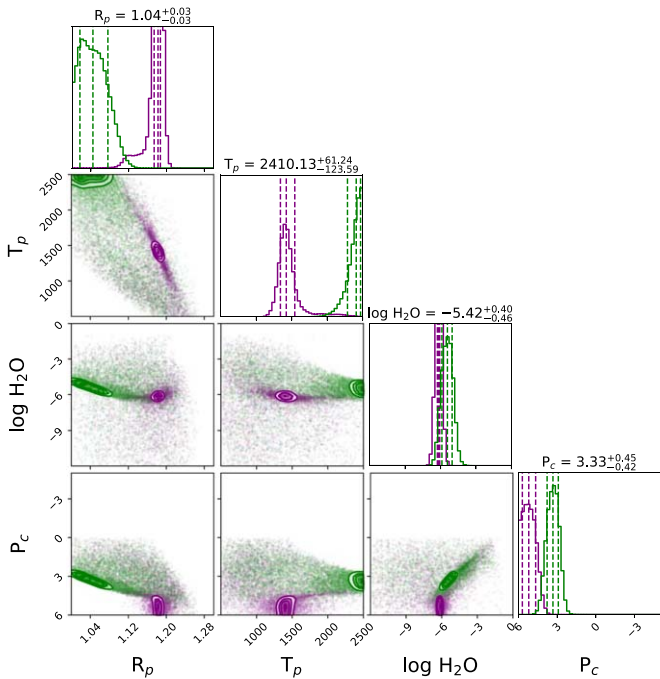


Figure 7. Posterior distributions from the water-only scenarios. Purple: water only; green: water only (no CIA).

of CO_2 and HCN (both around 10^{-3}), while CO cannot be confirmed. It is important to notice that, as demonstrated with the extended runs, the abundances for CO, CO_2 , and HCN are mainly driven by the points after $1.5 \mu\text{m}$. They thus present degeneracies and could be sensitive to random scatter of those data points. To properly confirm those abundances, other observations covering an additional independent feature of each of those molecules would be required, which could be provided by the next generation of telescopes. In this run, an opaque cloud cover is preferred in this solution, which might be compatible with the findings from Zák et al. (2019).

4. Discussion

As seen in the previous section, the example of KELT-11 b highlights how the choice of model can lead to different solutions and interpretations when performing atmospheric retrieval studies. In addition to this, when statistical methods are employed for model selection in HST data (e.g., comparison of Bayesian evidence), a better statistical evidence does not always guarantee that the favored model is the right one, since other unexplored scenarios might also provide a decent fit. This issue is a strong indication that retrieval studies should attempt to assess the information content in exoplanet spectra by exploring a wide enough range of scenarios. In our exploration, water vapor is robustly detected by all models, with subsolar abundances. As the water-only model provides a good fit to this spectrum, following the law of parsimony or Occam’s razor principle, one would be tempted to prefer this model. However, from a physical and chemical perspective, this model would imply that the atmosphere has an extremely low amount of water and is depleted in all other absorbing molecules in the wavelength considered. In this case, a model of higher complexity might provide a better description for this atmosphere. When carbon species are added, CO_2 is recovered with abundances that variate between 10^{-7} and 10^{-3} . CO and HCN are detected, depending on the choice of model and with

large posterior tails in the base and extended models. Those tails might be explained by the fact that the water-only model is already a good fit and by the similitude in the CO, CO_2 , and HCN contributions for the considered wavelength range. This could also indicate that the detection of carbon bearing species might be subject to systematic errors in the HST data, similar to what was found for VO in the case of WASP-121 b (Evans et al. 2017; Mikal-Evans et al. 2019). A larger wavelength coverage from additional observations might help resolve this issue.

In addition to model-dependent solutions, other aspects of retrieval studies could lead to different interpretations. In the first place, one can investigate the impact of using self-consistent schemes to represent chemical abundances. Furthermore, in the search for more precise characterizations, it is common to combine instrument observations, which in theory increase the information content on which to retrieve. However, such method can introduce systematic errors that should be investigated in the case of the TESS and HST data of KELT-11 b.

4.1. Comparison with an Equilibrium Scheme

Since HST observations have low information content, which typically only allow H_2O to be constrained, equilibrium chemistry models are also convenient to extrapolate the behavior of the other molecules. Importantly, their implied assumptions on the state of the planet and its physical/chemical behavior often neglect phenomena of major importance such as three-dimensional effect, dynamical effects, disequilibrium processes, to only name known sources of biases (Venot et al. 2015; Caldas et al. 2019; Changeat et al. 2019, 2020; Drummond et al. 2020). As the physics of such systems can be extremely complex and far from any environment we know in the solar system, the selection of a particular chemical model may lead to results biased by preconception. Nevertheless, it seems from our free exploration of the planet that carbon species might play an important role in shaping the WFC3 transmission spectrum of KELT-11 b, which could provide robust constraints to investigate equilibrium chemistry schemes for this planet. The posterior distribution and spectrum from our equilibrium chemistry run can be found in Figure 8.

For a more direct comparison, we also display the recovered abundances with altitude for this run in Figure 9. As can be seen in this figure, the dominant species in this atmosphere are H_2O , CO, and CO_2 , thus confirming the pertinence of our base scenario. We however note that the additional constraints from the assumption of equilibrium chemistry lead to higher abundances for those molecules, as can be inferred from the high retrieved metallicity of $\log M = 0.3^{+0.5}_{-0.7}$. The water abundance here is about 10^{-3} , which is closer to solar abundances than the free results. Other instances of high-metallicity atmospheres have already been observed in exoplanets (e.g., Wakeford et al. 2017; Spake et al. 2019; MacDonald & Madhusudhan 2019). A noticeable point is that the contribution from the more exotic carbon species added in the extended runs (HCN, C_2H_2 , and C_2H_4) remain minor when the equilibrium chemistry retrieval is used. Their recovered abundances are below 10^{-6} . Finally, the recovered abundances become about 10^{-6} . Finally, the recovered temperature becomes about 2400 K, which is higher than expected for this planet and might reflect remaining biases in this retrieval, especially as we can observe some evident correlations with other parameters. For comparison, we obtain $\Delta \log E = 59.3$,

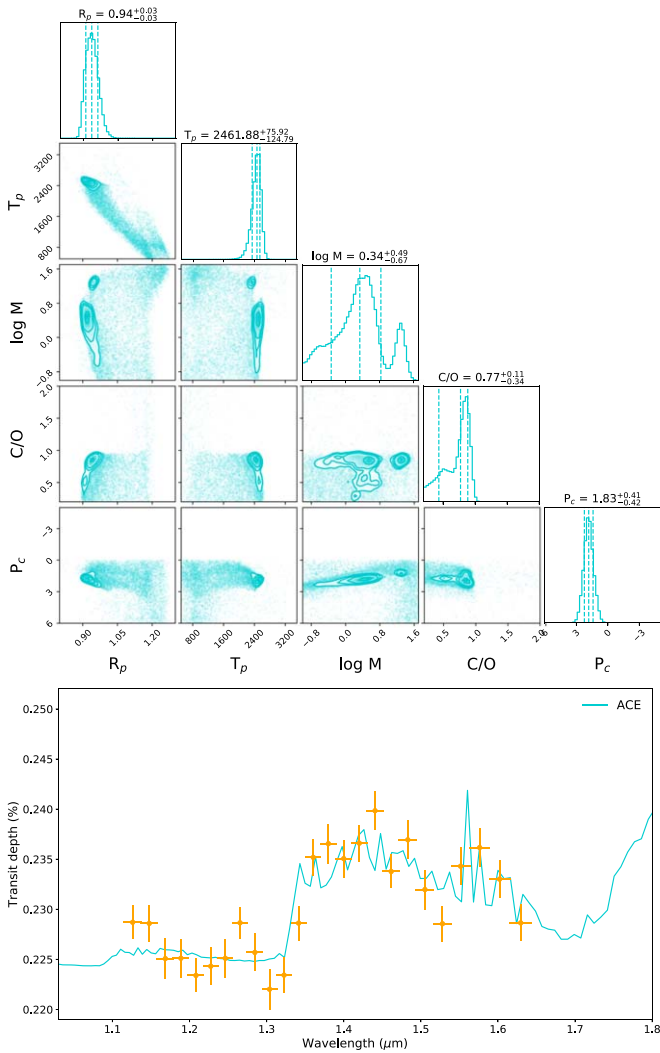


Figure 8. Posterior distribution (top) and best-fit spectrum (bottom) from the ACE scenario. This run assumes equilibrium chemistry using the scheme from Agúndez et al. (2014).

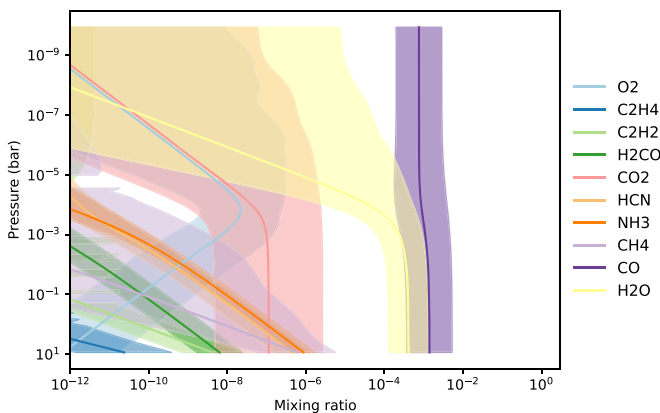


Figure 9. Mixing ratio with altitude of the active species in our ACE scenario.

which is much lower than any of the investigated free runs but help provide a sense of what one should expect in such a planet. This lower $\log E$ might however provide evidence that the assumption of equilibrium chemistry does not hold for this atmosphere.

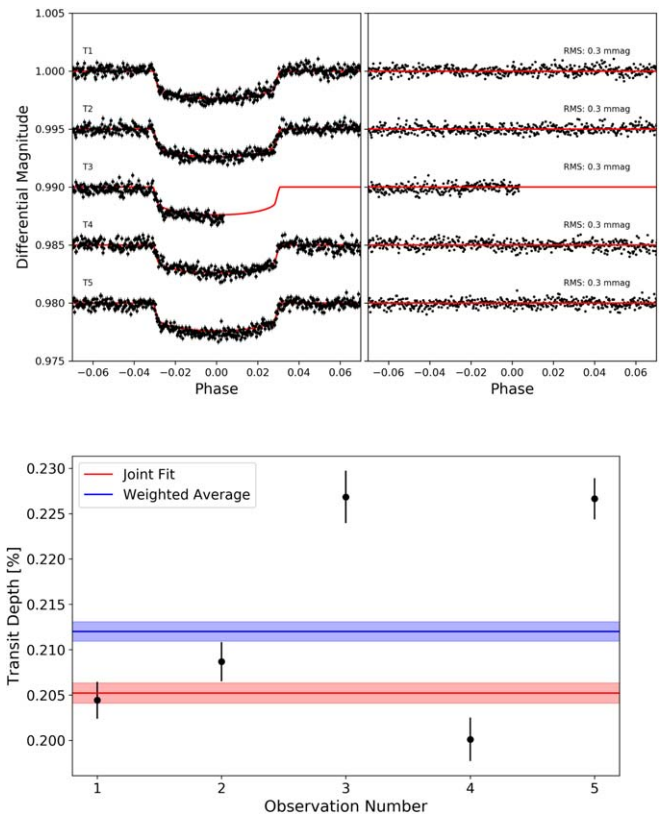


Figure 10. Top: fitting of the TESS observations presented in this work. Left: detrended data and best-fit model. Right: residuals from fitting. Bottom: recovered TESS depths for each transit (black) and from a joint fit of all the observations (red). The transit depth is seen to vary drastically. The weighted average of the individual fits is also shown (blue) and disagrees with the joint fit.

4.2. Impact of TESS in Retrieval Analyses

Motivated by the narrow wavelength coverage of the HST-G141 grism, many studies attempt to combine with other instruments, either adding the HST Space Telescope Imaging Spectrograph (STIS), Spitzer, TESS, and/or ground-based observations (e.g., Sing et al. 2016). In particular, Spitzer covers the CH_4 and the CO/CO_2 absorption bands with the photometric channels at $3.6 \mu\text{m}$ and $4.5 \mu\text{m}$. TESS and HST STIS cover shorter wavelengths, which are particularly sensitive to cloud/haze properties and absorption from atomic molecules and metal hydride/oxides (TiO , TiH , VO , and FeH , to name a few). However recent studies highlighted the danger of performing such combinations without investigating potential incompatibilities with the data sets (Pluriel et al. 2020; Yip et al. 2020, 2020). In particular, issues can arise when data sets are reduced using different orbital parameters (Alexoudi et al. 2018; Yip et al. 2020) or limb-darkening coefficients (Tsiaras et al. 2018). Furthermore, stellar variability and activity can produce spectra offsets when observations are not taken simultaneously (Bruno et al. 2020). Finally, imperfect correction of instrument systematics can lead to inconsistent results (Stevenson et al. 2014, 2017; Diamond-Lowe et al. 2014).

As explained previously, for KELT-11 b we discard entirely the available Spitzer data, due to the missing pre-ingress part of the transit. We however considered the addition of the TESS data since five transits were observed, making sure the orbital parameters and limb-darkening coefficients are consistent with the HST-G141 grism reduction. In Figure 10, we plot the

recovered TESS depths for each transit. As can be seen in this figure, there are large variations of the observed depths between the different transits.

These differences could come from variability in the environment (e.g., stellar activity, observation contamination) and/or imperfectly corrected systematics from the reduction. This leads to large differences whether we choose to combine the observations using a joint fit or a weighted average, confirming the difficulty of using TESS for atmospheric characterization in this case. We note that the third observation only covered half of the transit which may explain the discrepancy of this particular fit. When performing a retrieval analysis of a combined TESS and HST data set, many optical absorbers would have their posterior strongly defined by the TESS data, which could lead to biased results. In addition to this, when different reduction pipelines are used for HST-G141, the same spectrum shape is usually obtained but it is common to observe differences in the white light curve depth. Such an offset would only translate into biases for the radius when considering the HST data alone, but could lead to unstable results when combining with other instruments.

Fully aware of these potential incompatibilities, we added the obtained TESS joint fit/weighted averaged and performed an atmospheric retrieval similar to our full scenario. The results from those retrievals, which are available in Appendix E, highlight possible incompatibilities between the two data sets, as discussed above. Both solutions, from the joint fit and the weighted averaged TESS data, lead to nonphysical solutions with high abundances of H₂O and either HCN or CO₂. It is interesting to see that the low observed TESS photometric point leads to the replacement of TiO by FeH in those runs. Those retrievals are good examples illustrating why extra care might be required when combining instrument observations in retrieval studies. In the case of KELT-11 b, the data sets may have been made incompatible due to uncorrected systematics in the HST data as the white light curve residuals seen here, and in Colón et al. (2020), are non-Gaussian.

To understand if there is indeed an offset between these data sets, further data is required. While STIS data has not been acquired for this planet, G102 will soon be obtained (PN: 15926, PI: Knicole Colon; Colon et al. 2019) and provide further insights into the nature of this planet, helping to distinguish between the potential compositions presented here.

4.3. Comparison with Other Literature Results

The same data set from the HST G141 grism was recently analyzed in an independent study from Colón et al. (2020). While different reduction pipelines were used, their main conclusions are similar to ours, unveiling a spectrum with similar spectral shape to what is presented here. The studies strongly agree on the presence of water vapor in this planet, with subsolar abundances that vary depending on model assumptions. Due to the shape of the spectrum, the need for an additional absorption after 1.5 μm is also highlighted. In Colón et al. (2020), this is attributed to HCN. In our study, we show this could be well matched by a mix of carbon bearing species, which include HCN, but we were not able to statistically attribute the features to this molecule only (see Table 2). The evidence for TiO is highlighted in Colón et al. (2020), which is strongly confirmed by their addition of the TESS data. However, as mentioned in the previous section, the combination of data sets from different instruments with no wavelength

overlap should be done carefully. In particular, our spectrum, while having a similar spectral shape, is offset by about 200 ppm to the one used in Colón et al. (2020). Similar offsets of about 400 ppm are also observed in their paper as well, when analyzing the spectra obtained with different pipelines. In our full retrieval, which includes TiO as well as other near-visible species, we find that TiO is also favored in the HST data set (this is driven by the data points around 1.3 μm), but when the TESS data is added, TiO disappears in favor of FeH, due to the higher HST spectrum recovered in our study. Thus, identification of a near-visible absorber and/or its precise abundance is likely to be biased by systematic offsets when TES and HST is used. Finally, most of our retrievals recover a well-defined temperature around 1300 K, which is expected from previous transit observations (Tsiaras et al. 2018; Caldas et al. 2019; MacDonald et al. 2020; Pluriel et al. 2020; Skaf et al. 2020). However, this disagrees with the findings from Colón et al. (2020), which find a lower limit on the temperature of about 1900 K. These differences could either be due to the use of different reduction/retrieval pipelines or differences in the choice of models (temperature/clouds).

5. Conclusion

Having one of the highest signal-to-noise ratios of the known exoplanets and a super extended atmosphere, KELT-11 b will be a prime target for future observatories. We analyzed the HST G141 spectrum of the planet KELT-11 b. From our spectral retrieval exploration, we confirmed the presence of water vapor, with subsolar abundances. In addition to this, the rich spectrum features an additional absorption after 1.5 μm , which is clearly detected in all our retrieval scenarios. This could come from a mixture of carbon bearing species (CO, CO₂, or HCN) and while equilibrium chemistry seem to favor CO and CO₂, the spectrum does not contain enough information to clearly identify the mix of compounds. However, when included, CO₂ seems to be systematically detected, with varying abundances depending on the model. The high abundance of carbon species, inferred from the base model, and the relatively low abundance of water suggest a planet with a high C/O ratio (Venot et al. 2015). This could have important implications regarding the formation processes for this planet and potential formation and evolution models (Öberg et al. 2011). A high C/O ratio, along with the contrast between our rich spectrum and the data from the ground at shorter wavelengths (Zák et al. 2019), showcases a planet with particularly interesting physics and chemistry. Observations with future observatories, such as the James Webb Space Telescope (Greene et al. 2016), Twinkle (Edwards et al. 2018), and the Atmospheric Remote-sensing Infrared Exoplanet Large-survey (ARIEL; Tinetti et al. 2018), would dramatically enhance our comprehension of this world and thus provide outstanding information for chemical models and formation theories.

Using this planet as an example, we explored model-dependent behavior in retrieval analysis and highlighted the dangers of assuming a particular physics (self-consistent schemes) when trying to extract information content from exoplanet spectra. We also experimented the behavior of retrieval analyses on a combined data set, by adding the available TESS data to our HST spectrum of KELT-11 b.

This project has received funding from the European Research Council (ERC) under the European Union’s Horizon 2020 research and innovation program (grant agreement No. 758892, ExoAI) and under the European Union’s Seventh Framework Programme (FP7/2007-2013)/ ERC grant agreement Nos. 617119 (ExoLights). Furthermore, we acknowledge funding by the Science and Technology Funding Council (STFC) grants: ST/K502406/1, ST/P000282/1, ST/P002153/1, ST/S002634/1, and ST/T001836/1.

We acknowledge the availability and support from the High Performance Computing platforms (HPC) DIRAC and OzSTAR, which provided the computing resources necessary to perform this work.

This work is based on observations made with the NASA/ESA Hubble Space Telescope. These publicly available observations were taken as part of proposal 15225, led by Knicole Colon (Colon 2017). These were obtained from the Hubble Archive which is part of the Barbara A. Mikulski Archive for Space Telescopes. Additionally, this paper includes data collected by the TESS mission which is funded by the

NASA Explorer Program. TESS data is also publicly available via the Barbara A. Mikulski Archive for Space Telescopes (MAST). We are thankful to those who operate this archive, the public nature of which increases scientific productivity and accessibility (Peek et al. 2019).

Software: corner (Foreman-Mackey 2016), Iraclis (Tsiaras et al. 2016b), TauREx3 (Al-Refaie et al. 2019), pylightcurve (Tsiaras et al. 2016), ExoTETHyS (Morello et al. 2020), Astropy (Astropy Collaboration et al. 2018), h5py (Collette 2013), emcee (Foreman-Mackey et al. 2013), Matplotlib (Hunter 2007), Multinest (Feroz et al. 2009), Pandas (McKinney 2011), Numpy (Oliphant 2006), SciPy (Virtanen et al. 2020).

Appendix A Parameters and Limb-darkening Coefficients Used in This Work

The list of parameters and limb-darkening coefficients that are used in this work are summarized respectively in Tables 3 and 4.

Table 3
Parameters Used in This Work from Beatty et al. (2017)

Parameter	Value	Unit
Stellar Parameters		
Radius (R_s)	2.69 ± 0.22	R_\odot
Mass (M_s)	1.44 ± 0.43	M_\odot
Temperature (T_s)	5375 ± 25	K
Surface gravity ($\log g$)	3.7 ± 0.1	cgs
Metallicity ($[Fe/H]$)	0.17 ± 0.07	...
Orbital Parameters		
Transit mid-time (T_0)	2457483.431 ± 0.0007	BJD_{TDB}
Period (P)	4.73613 ± 0.00003	days
Inclination (i)	85.3 ± 0.3	degrees
Semimajor-axis-to-star-radius ratio (a/R_s)	4.98 ± 0.05	...
Eccentricity (e)	$0.0007^{+0.002}_{-0.0005}$...
Planet Parameters		
Radius (R_p)	1.35 ± 0.10	R_J
Mass (M_p)	0.171 ± 0.015	M_J

Table 4
Limb-darkening Coefficients Used During Light Curve Fitting

Wavelength [μm]	c1	c2	c3	c4
1.1153-1.1372	0.4729	-0.0342	0.2561	-0.1297
1.1372-1.1583	0.4532	0.0230	0.2024	-0.1152
1.1583-1.1789	0.4583	0.0242	0.1844	-0.1081
1.1789-1.1987	0.4508	0.0545	0.1499	-0.0976
1.1987-1.2180	0.4453	0.0679	0.1339	-0.0928
1.2180-1.2370	0.4346	0.1111	0.0897	-0.0801
1.2370-1.2559	0.4340	0.1239	0.0710	-0.0743
1.2559-1.2751	0.4231	0.1646	0.0266	-0.0609
1.2751-1.2944	0.4216	0.2388	-0.0943	-0.0180
1.2944-1.3132	0.4060	0.2362	-0.0572	-0.0338
1.3132-1.3320	0.4108	0.2483	-0.0812	-0.0252
1.3320-1.3509	0.4035	0.2913	-0.1378	-0.0050
1.3509-1.3701	0.4035	0.3216	-0.1822	0.0108
1.3701-1.3900	0.4151	0.3198	-0.2017	0.0202
1.3900-1.4100	0.4319	0.3159	-0.2135	0.0241
1.4100-1.4303	0.4105	0.3725	-0.2713	0.0434
1.4303-1.4509	0.4341	0.3518	-0.2740	0.0466
1.4509-1.4721	0.4648	0.3302	-0.2903	0.0577
1.4721-1.4941	0.5310	0.2144	-0.2116	0.0363
1.4941-1.5165	0.5683	0.1675	-0.2020	0.0395
1.5165-1.5395	0.6338	0.0681	-0.1479	0.0281
1.5395-1.5636	0.6217	0.1085	-0.2146	0.0576
1.5636-1.5889	0.6454	0.0502	-0.1806	0.0526
1.5889-1.6153	0.6937	-0.0577	-0.0897	0.0221
1.6153-1.6436	0.7903	-0.2637	0.0857	-0.0332

Appendix B

Extracted Spectrum for KELT-11 b

Table 5 provides the extracted spectrum from KELT-11 b.

Table 5
WFC3 Transit Depths and Errors (in Percent) for for KELT-11 b

Wavelength [μm]	Transit depth [%]	Error [%]
1.1153-1.1372	0.22871	0.00161
1.1372-1.1583	0.22859	0.00177
1.1583-1.1789	0.22508	0.00196
1.1789-1.1987	0.22511	0.00189
1.1987-1.2180	0.22340	0.00162
1.2180-1.2370	0.22432	0.00179
1.2370-1.2559	0.22511	0.00188
1.2559-1.2751	0.22866	0.00150
1.2751-1.2944	0.22570	0.00181
1.2944-1.3132	0.22202	0.00197
1.3132-1.3320	0.22343	0.00173
1.3320-1.3509	0.22862	0.00165
1.3509-1.3701	0.23519	0.00177
1.3701-1.3900	0.23655	0.00190
1.3900-1.4100	0.23506	0.00182
1.4100-1.4303	0.23660	0.00176
1.4303-1.4509	0.23985	0.00185
1.4509-1.4721	0.23378	0.00162
1.4721-1.4941	0.23694	0.00186
1.4941-1.5165	0.23197	0.00190
1.5165-1.5395	0.22856	0.00172
1.5395-1.5636	0.23431	0.00183
1.5636-1.5889	0.23617	0.00189
1.5889-1.6153	0.23302	0.00180
1.6153-1.6436	0.22865	0.00176

Appendix C Contributions of Absorbing Species to the Best-fit Models

Figure 11 shows the contribution of different absorbing species to the best fit models of KELT-11 b.

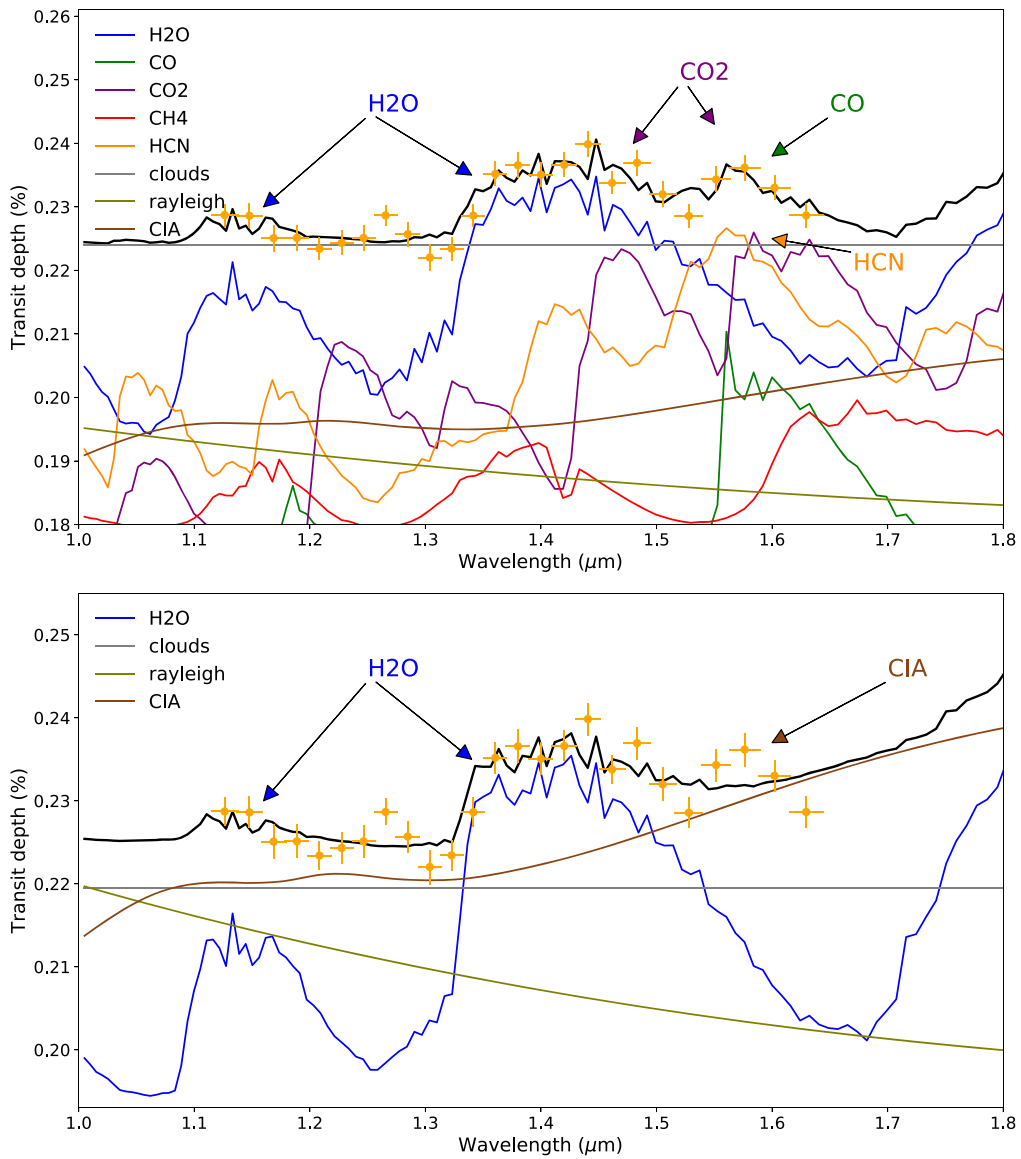


Figure 11. Best-fit contributions from the different absorbing species for the Solution 1 of the extended scenario (top) and the water-only retrievals (bottom).

Appendix D Posterior Distributions of the Full Model

The posterior distribution of the full model is described in Figure 12.

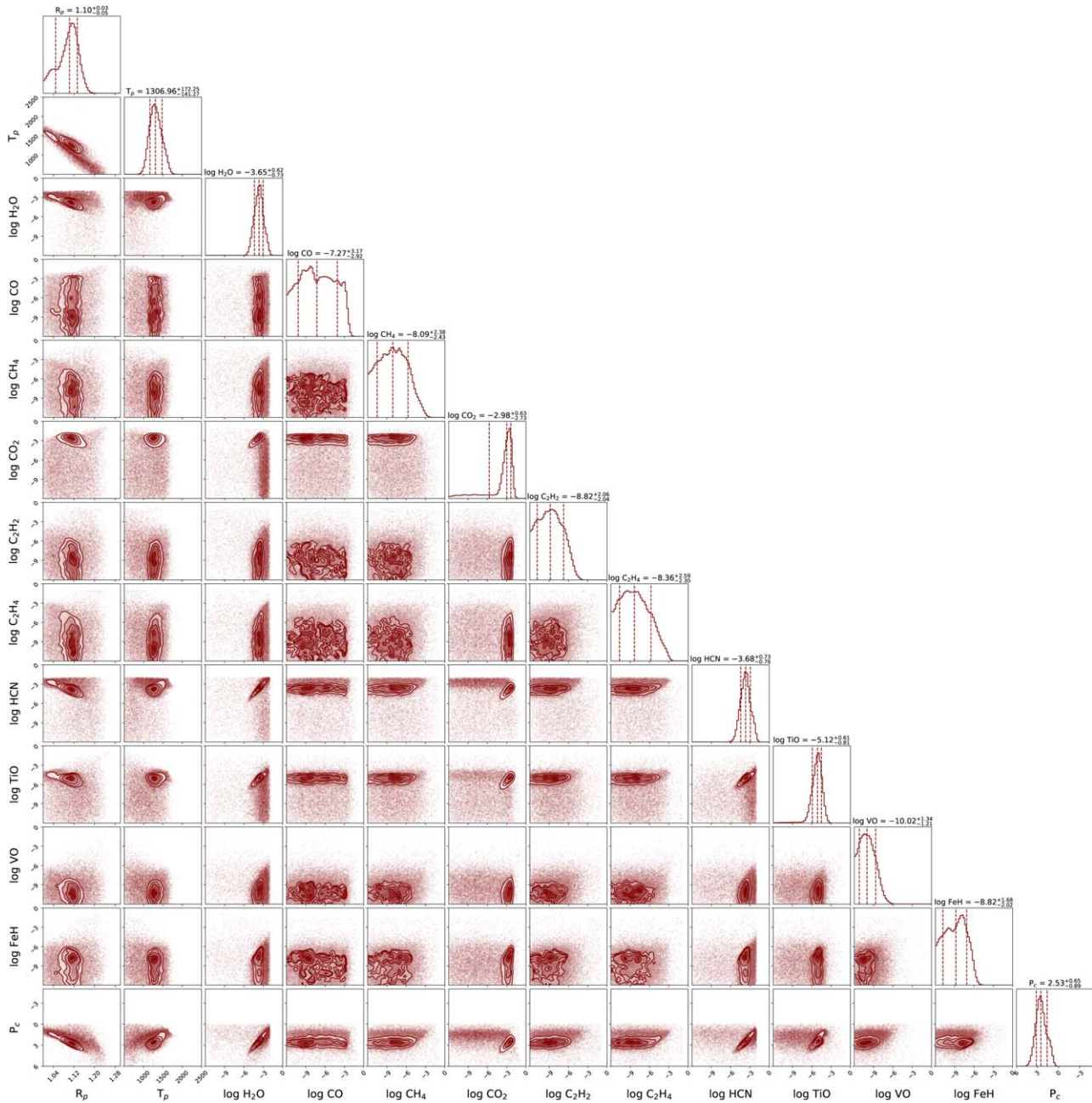


Figure 12. Posterior distribution of the full model, which includes the full range of carbon bearing species and the near-optical absorbers TiO, VO, and FeH.

Appendix E

Results of the Combined Retrievals

The result of our combined retrievals are shown in Figures 13 and 14 for the spectra and posteriors.

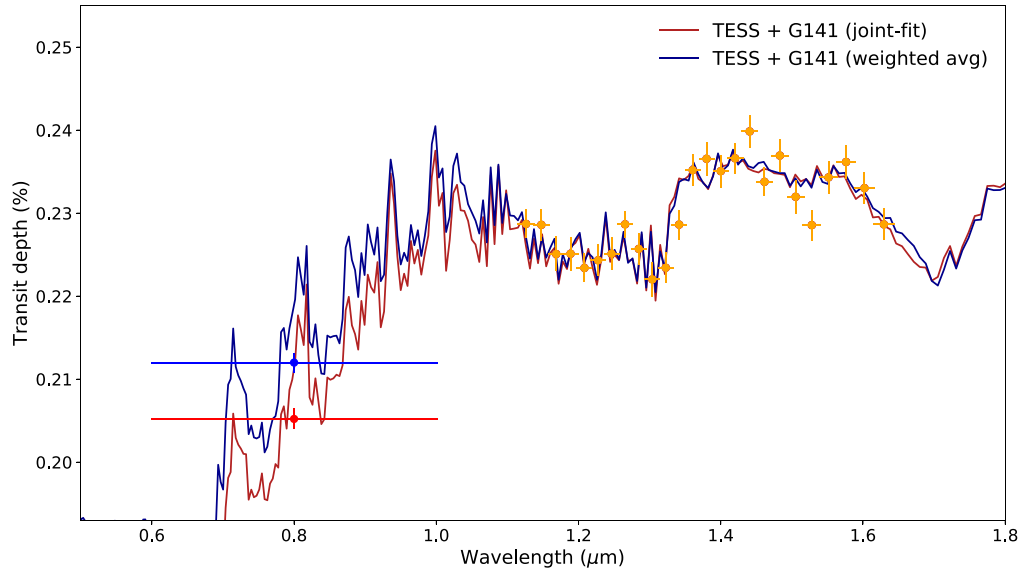


Figure 13. Best-fit spectra for the combined retrievals of TESS and HST. Red: retrieval using the joint fit of the TESS data; blue: retrieval using the weighted averaged TESS data.

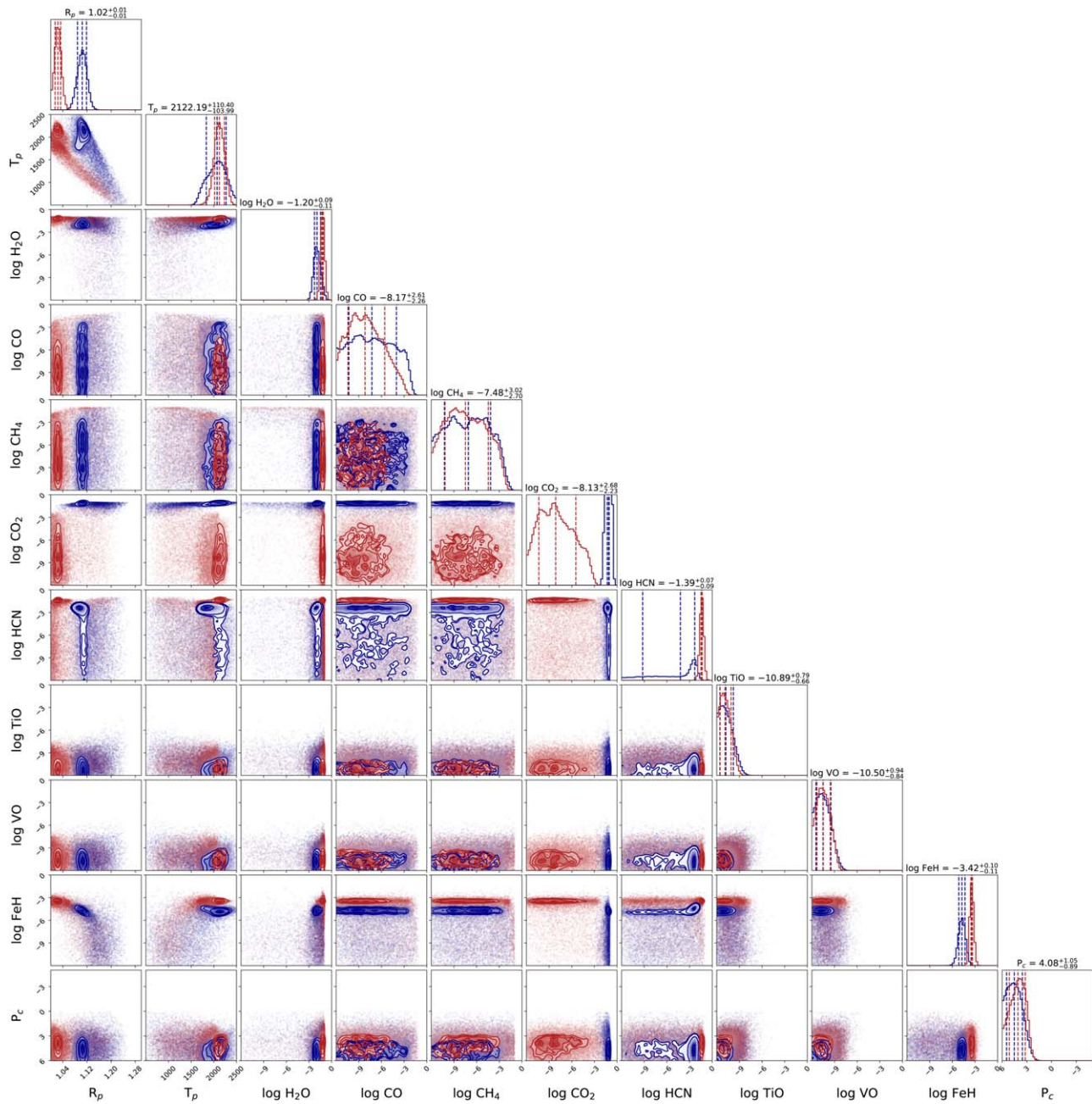


Figure 14. Posterior distribution for the combined retrievals of TESS and HST. Red: retrieval using the joint fit of the TESS data; blue: retrieval using the weighted averaged TESS data.

ORCID iDs

Q. Changeat <https://orcid.org/0000-0001-6516-4493>
 B. Edwards <https://orcid.org/0000-0002-5494-3237>
 A. F. Al-Refaie <https://orcid.org/0000-0003-2241-5330>
 M. Morvan <https://orcid.org/0000-0001-8587-2112>
 A. Tsiaras <https://orcid.org/0000-0003-3840-1793>
 I. P. Waldmann <https://orcid.org/0000-0002-4205-5267>
 G. Tinetti <https://orcid.org/0000-0001-6058-6654>

References

Abel, M., Frommhold, L., Li, X., & Hunt, K. L. 2011, *JPCA*, **115**, 6805
 Abel, M., Frommhold, L., Li, X., & Hunt, K. L. 2012, *JChPh*, **136**, 044319
 Agol, E., Cowan, N. B., Knutson, H. A., et al. 2010, *ApJ*, **721**, 1861

Agúndez, M., Parmentier, V., Venot, O., Hersant, F., & Selsis, F. 2014, *A&A*, **564**, A73
 Alexoudi, X., Mallonn, M., von Essen, C., et al. 2018, *A&A*, **620**, A142
 Allard, F., Homeier, D., & Freytag, B. 2012, *RSPTA*, **370**, 2765
 Al-Refaie, A. F., Changeat, Q., Waldmann, I. P., & Tinetti, G. 2019, arXiv:1912.07759
 Anisman, L. O., Edwards, B., Changeat, Q., et al. 2020, *AJ*, **160**, 233
 Astropy Collaboration, Price-Whelan, A. M., Sipőcz, B. M., et al. 2018, *AJ*, **156**, 18
 Barber, R. J., Strange, J. K., Hill, C., et al. 2013, *MNRAS*, **437**, 1828
 Barman, T. S., Konopacky, Q. M., Macintosh, B., & Marois, C. 2015, *ApJ*, **804**, 61
 Barstow, J. K., Aigrain, S., Irwin, P. G. J., & Sing, D. K. 2017, *ApJ*, **834**, 50
 Barstow, J. K., Changeat, Q., Garland, R., et al. 2020, *MNRAS*, **493**, 4884
 Barton, E. J., Hill, C., Yurchenko, S. N., et al. 2017, *JQSRT*, **187**, 453
 Beatty, T. G., Stevens, D. J., Collins, K. A., et al. 2017, *AJ*, **154**, 25
 Bernath, P. F. 2020, *JQSRT*, **240**, 106687

- Brogi, M., Line, M., Bean, J., Désert, J.-M., & Schwarz, H. 2017, *ApJL*, **839**, L2
- Brogi, M., & Line, M. R. 2019, *AJ*, **157**, 114
- Bruno, G., Lewis, N. K., Alam, M. K., et al. 2020, *MNRAS*, **491**, 5361
- Caldas, A., Leconte, J., Selsis, F., et al. 2019, *A&A*, **623**, A161
- Changeat, Q., & Al-Refaie, A. 2020, *ApJ*, **898**, 155
- Changeat, Q., Al-Refaie, A., Mugnai, L. V., et al. 2020, *AJ*, **160**, 80
- Changeat, Q., Al-Refaie, A. F., Edwards, B., Waldmann, I. P., & Tinetti, G. 2020, *AJ*, **160**, 80
- Changeat, Q., Edwards, B., Waldmann, I. P., & Tinetti, G. 2019, *ApJ*, **886**, 39
- Changeat, Q., Keyte, L., Waldmann, I. P., & Tinetti, G. 2020, *ApJ*, **896**, 107
- Chubb, K. L., Rocchetto, M., Yurchenko, S. N., et al. 2020, arXiv:2009.00687
- Collette, A. 2013, Python and HDF5 (Sebastopol, CA: O'Reilly)
- Colon, K. 2017, The KELT-11b Opportunity: Measuring the Atmospheric Water Abundance for a Sub-Saturn-Mass Planet around a Metal-Rich Star, HST Proposal, [id. 15255](#)
- Colon, K., Angerhausen, D., Barclay, T., et al. 2019, Testing the Hypothesis of a Low Metallicity Atmosphere for the Extremely Inflated Sub-Saturn-Mass Planet KELT-11b, HST Proposal, [id. 15926](#)
- Colón, K. D., Kreidberg, L., Line, M., et al. 2020, *AJ*, submitted (arXiv:2005.05153)
- Cox, A. N. 2015, *Allen's Astrophysical Quantities* (Berlin: Springer)
- Crouzet, N., McCullough, P. R., Deming, D., & Madhusudhan, N. 2014, *ApJ*, **795**, 166
- de Kok, R., Brogi, M., Snellen, I., et al. 2013, *A&A*, **554**, A82
- Deming, D., Wilkins, A., McCullough, P., et al. 2013, *ApJ*, **774**, 95
- Diamond-Lowe, H., Stevenson, K. B., Bean, J. L., Line, M. R., & Fortney, J. J. 2014, *ApJ*, **796**, 66
- Drummond, B., Hébrard, E., Mayne, N. J., et al. 2020, *A&A*, **636**, A68
- Edwards, B., Changeat, Q., Baeyens, R., et al. 2020a, *AJ*, **160**, 8
- Edwards, B., Changeat, Q., Yip, K. H., et al. 2020b, *MNRAS*, in press
- Edwards, B., Rice, M., Zingales, T., et al. 2018, *ExA*, **47**, 29
- Evans, T. M., Sing, D. K., Kataria, T., et al. 2017, *Natur*, **548**, 58
- Evans, T. M., Sing, D. K., Wakeford, H. R., et al. 2016, *ApJL*, **822**, L4
- Feng, Y. K., Line, M. R., Fortney, J. J., et al. 2016, *ApJ*, **829**, 52
- Feng, Y. K., Line, M. R., & Fortney, J. J. 2020, *AJ*, **160**, 137
- Feroz, F., Hobson, M. P., & Bridges, M. 2009, *MNRAS*, **398**, 1601
- Foreman-Mackey, D. 2016, *JOSS*, **1**, 24
- Foreman-Mackey, D., Hogg, D. W., Lang, D., & Goodman, J. 2013, *PASP*, **125**, 306
- Fu, G., Deming, D., Knutson, H., et al. 2017, *ApJL*, **847**, L22
- Gandhi, S., Madhusudhan, N., Hawker, G., & Piette, A. 2019, *AJ*, **158**, 228
- Greene, T. P., Line, M. R., Montero, C., et al. 2016, *ApJ*, **817**, 17
- Harris, G. J., Tennyson, J., Kaminsky, B. M., Pavlenko, Y. V., & Jones, H. R. A. 2006, *MNRAS*, **367**, 400
- Hill, C., Yurchenko, S. N., & Tennyson, J. 2013, *Icar*, **226**, 1673
- Hunter, J. D. 2007, *CSE*, **9**, 90
- Irwin, P. G. J., Parmentier, V., Taylor, J., et al. 2020, *MNRAS*, **493**, 106
- Irwin, P. G. J., Teanby, N. A., de Kok, R., et al. 2008, *JQSRT*, **109**, 1136
- Kass, R. E., & Raftery, A. E. 1995, *J. Am. Stat. Assoc.*, **90**, 773
- Konopacky, Q. M., Barman, T. S., Macintosh, B. A., & Marois, C. 2013, *Sci*, **339**, 1398
- Kreidberg, L., Bean, J. L., Désert, J.-M., et al. 2014, *Natur*, **505**, 69
- Kreidberg, L., Line, M. R., Bean, J. L., et al. 2015, *ApJ*, **814**, 66
- Lacour, S., Nowak, M., Wang, J., et al. 2019, *A&A*, **623**, L11
- Li, G., Gordon, I. E., Rothman, L. S., et al. 2015, *ApJS*, **216**, 15
- Line, M. R., Stevenson, K. B., Bean, J., et al. 2016, *AJ*, **152**, 203
- Line, M. R., Wolf, A. S., Zhang, X., et al. 2013, *ApJ*, **775**, 137
- MacDonald, R. J., Goyal, J. M., & Lewis, N. K. 2020, *ApJL*, **893**, L43
- MacDonald, R. J., & Madhusudhan, N. 2019, *MNRAS*, **486**, 1292
- Macintosh, B., Graham, J. R., Barman, T., et al. 2015, *Sci*, **350**, 64
- Madhusudhan, N., Harrington, J., Stevenson, K. B., et al. 2010, *Natur*, **469**, 64
- Madhusudhan, N., & Seager, S. 2009, *ApJ*, **707**, 24
- Mant, B. P., Yachmenev, A., Tennyson, J., & Yurchenko, S. N. 2018, *MNRAS*, **478**, 3220
- McCullough, P., & MacKenty, J. 2012, Considerations for Using Spatial Scans with WFC3, WFC Instrument Science Rep., [WFC3 2012-08](#)
- McKemmish, L. K., Masseron, T., Hoeijmakers, H. J., et al. 2019, *MNRAS*, **488**, 2836
- McKemmish, L. K., Yurchenko, S. N., & Tennyson, J. 2016, *MNRAS*, **463**, 771
- McKinney, W. 2011, Python for High Performance and Scientific Computing, **14**, 9, https://www.dlr.de/sc/portaldata/15/resources/dokumente/pyhpc2011/submissions/pyhpc2011_submission_9.pdf
- Mikal-Evans, T., Sing, D. K., Goyal, J. M., et al. 2019, *MNRAS*, **488**, 2222
- Min, M., Ormel, C. W., Chubb, K., Helling, C., & Kawashima, Y. 2020, *A&A*, **642**, A28
- Mollière, P., Wardenier, J. P., van Boekel, R., et al. 2019, *A&A*, **627**, A67
- Morello, G., Claret, A., Martin-Lagarde, M., et al. 2020, *AJ*, **159**, 75
- Morvan, M., Nikolaou, N., Tsiaras, A., & Waldmann, I. P. 2020, *AJ*, **159**, 109
- Öberg, K. I., Murray-Clay, R., & Bergin, E. A. 2011, *ApJL*, **743**, L16
- Oliphant, T. E. 2006, *A Guide to NumPy*, Vol. 1 (Spanish Fork, UT: Trelgol Publishing)
- Parmentier, V., Line, M. R., Bean, J. L., et al. 2018, *A&A*, **617**, A110
- Peek, J., Desai, V., White, R. L., et al. 2019, *BAAS*, **51**, 105
- Pepper, J., Rodriguez, J. E., Collins, K. A., et al. 2017, *AJ*, **153**, 215
- Pinhas, A., Madhusudhan, N., Gandhi, S., & MacDonald, R. 2019, *MNRAS*, **482**, 1485
- Pluriel, W., Whiteford, N., Edwards, B., et al. 2020, *AJ*, **160**, 112
- Pluriel, W., Zingales, T., Leconte, J., & Parmentier, V. 2020, *A&A*, **636**, A66
- Polyansky, O. L., Kyuberis, A. A., Zobov, N. F., et al. 2018, *MNRAS*, **480**, 2597
- Ricker, G. R., Winn, J. N., Vanderspek, R., et al. 2014, *Proc. SPIE*, **9143**, 914320
- Rocchetto, M., Waldmann, I. P., Venot, O., Lagage, P. O., & Tinetti, G. 2016, *ApJ*, **833**, 120
- Rodgers, C. D. 2000, *Inverse Methods for Atmospheric Sounding—Theory and Practice: Series on Atmospheric Oceanic and Planetary Physics* (Singapore: World Scientific)
- Rothman, L., Gordon, I., Barber, R., et al. 2010, *JQSRT*, **111**, 2139
- Sing, D. K., Fortney, J. J., Nikolov, N., et al. 2016, *Natur*, **529**, 59
- Skaf, N., Bieger, M. F., Edwards, B., et al. 2020, *AJ*, **160**, 109
- Smith, J. C., Stumpe, M. C., van Cleve, J. E., et al. 2012, *PASP*, **124**, 1000
- Snellen, I. A. G., de Kok, R. J., de Mooij, E. J. W., & Albrecht, S. 2010, *Natur*, **465**, 1049
- Spake, J. J., Sing, D. K., Wakeford, H. R., et al. 2019, *MNRAS*, in press
- Stevenson, K. B., Désert, J.-M., Line, M. R., et al. 2014, *Sci*, **346**, 838
- Stevenson, K. B., Line, M. R., Bean, J. L., et al. 2017, *AJ*, **153**, 68
- Stumpe, M. C., Smith, J. C., Catanzarite, J. H., et al. 2014, *PASP*, **126**, 100
- Stumpe, M. C., Smith, J. C., van Cleve, J. E., et al. 2012, *PASP*, **124**, 985
- Swain, M. R., Tinetti, G., Vasisth, G., et al. 2009, *ApJ*, **704**, 1616
- Swain, M. R., Vasisth, G., Tinetti, G., et al. 2008, *ApJL*, **690**, L114
- Tennyson, J., & Yurchenko, S. N. 2012, *MNRAS*, **425**, 21
- Tennyson, J., Yurchenko, S. N., Al-Refaie, A. F., et al. 2016, *JMoSp*, **327**, 73
- Tennyson, J., Yurchenko, S. N., Al-Refaie, A. F., et al. 2020, *JQSRT*, **255**, 107228
- Tinetti, G., Drossart, P., Eccleston, P., et al. 2018, *ExA*, **46**, 135
- Tinetti, G., Vidal-Madjar, A., Liang, M.-C., et al. 2007, *Natur*, **448**, 169
- Tsiaras, A., Rocchetto, M., Waldmann, I. P., et al. 2016a, *ApJ*, **820**, 99
- Tsiaras, A., Waldmann, I., Rocchetto, M., et al. 2016, *pylightcurve: Exoplanet Lightcurve Model, Astrophysics Source Code Library*, [ascl:1612.018](#)
- Tsiaras, A., Waldmann, I. P., Rocchetto, M., et al. 2016b, *ApJ*, **832**, 202
- Tsiaras, A., Waldmann, I. P., Tinetti, G., Tennyson, J., & Yurchenko, S. N. 2019, *NatAs*, **3**, 1086
- Tsiaras, A., Waldmann, I. P., Zingales, T., et al. 2018, *AJ*, **155**, 156
- Venot, O., Hébrard, E., Agúndez, M., Decin, L., & Bounameaux, R. 2015, *A&A*, **577**, A33
- Virtanen, P., Gommers, R., Oliphant, T. E., et al. 2020, *NatMe*, **17**, 261
- Wakeford, H. R., Sing, D. K., Deming, D., et al. 2017, *AJ*, **155**, 29
- Waldmann, I. P., Rocchetto, M., Tinetti, G., et al. 2015a, *ApJ*, **813**, 13
- Waldmann, I. P., Tinetti, G., Rocchetto, M., et al. 2015b, *ApJ*, **802**, 107
- Wilzewski, J. S., Gordon, I. E., Kochanov, R. V., Hill, C., & Rothman, L. S. 2016, *JQSRT*, **168**, 193
- Yip, K. H., Changeat, Q., Edwards, B., et al. 2020, arXiv:2009.10438
- Yip, K. H., Waldmann, I. P., Tsiaras, A., & Tinetti, G. 2020, *AJ*, **160**, 171
- Yurchenko, S. N., & Tennyson, J. 2014, *MNRAS*, **440**, 1649
- Zák, J., Kabáth, P., Boffin, H. M. J., Ivanov, V. D., & Skarka, M. 2019, *AJ*, **158**, 120
- Zhang, M., Chachan, Y., Kempton, E. M. R., & Knutson, H. A. 2019, *PASP*, **131**, 034501